



# The Effects of Circumstellar Dust Scattering on the Light Curves and Polarizations of Type Ia Supernovae\*

Maokai Hu<sup>1,2</sup>, Lifan Wang<sup>3</sup>, and Xiaofeng Wang<sup>4,5</sup><sup>1</sup> Purple Mountain Observatory, Chinese Academy of Sciences, Nanjing 210023, People's Republic of China; [kaihukaihu123@pmo.ac.cn](mailto:kaihukaihu123@pmo.ac.cn)<sup>2</sup> School of Astronomy and Space Science, University of Science and Technology of China, Hefei, Anhui 230026, People's Republic of China<sup>3</sup> George P. and Cynthia Woods Mitchell Institute for Fundamental Physics & Astronomy, Texas A&M University, Department of Physics and Astronomy, 4242 TAMU, College Station, TX 77843, USA; [lifan@tamu.edu](mailto:lifan@tamu.edu)<sup>4</sup> Physics Department and Tsinghua Center for Astrophysics (THCA), Tsinghua University, Beijing, 100084, People's Republic of China<sup>5</sup> Beijing Planetarium, Beijing Academy of Science and Technology, Beijing, 100044, People's Republic of China

Received 2021 August 31; revised 2022 April 14; accepted 2022 April 28; published 2022 June 1

## Abstract

Observational signatures of the circumstellar material (CSM) around Type Ia supernovae (SNe Ia) provide a unique perspective on their progenitor systems. The pre-supernova evolution of the SN progenitors may naturally eject CSM in most of the popular scenarios of SN Ia explosions. In this study, we investigate the influence of dust scattering on the light curves and polarizations of SNe Ia. A Monte Carlo method is constructed to numerically solve the process of radiative transfer through the CSM. Three types of geometric distributions of the CSM are considered: spherical shell, axisymmetric disk, and axisymmetric shell. We show that both the distance of the dust from the SN and the geometric distribution of the dust affect the light curve and color evolutions of SN. We found that the geometric location of the hypothetical circumstellar dust may not be reliably constrained based on photometric data alone, even for the best observed cases such as SN 2006X and SN 2014J, due to the degeneracy of CSM parameters. Our model results show that a time sequence of broadband polarimetry with appropriate time coverage from a month to about one year after explosion can provide unambiguous limits on the presence of circumstellar dust around SNe Ia.

*Unified Astronomy Thesaurus concepts:* Type Ia supernovae (1728); Light curves (918)

## 1. Introduction

Type Ia supernovae (SNe Ia) have well-defined light curves and are employed empirically as cosmological distance indicators (Riess et al. 1998, 2007; Perlmutter et al. 1999; Wang et al. 2003; He et al. 2018). Of particular interest is the nature of their progenitor systems (e.g., Howell 2011; Maoz et al. 2014). Theoretically there are two major channels, and both involve white dwarfs (WDs) in binary systems (e.g., Hillebrandt & Niemeyer 2000). In the single degenerate channel the WD accretes matter from a nondegenerate star to reach the critical mass for SN explosion (Whelan & Iben 1973; Nomoto 1982), whereas in the double degenerate channel the explosion is achieved by the merging of the WD with a degenerate companion (Iben & Tutukov 1984; Webbink 1984). In either case, circumstellar material (CSM) may be ejected before the explosion, and studies of this may provide unique clues to the nature of the progenitors of SNe Ia (Förster et al. 2012; Shen et al. 2013; Yang et al. 2017; Li et al. 2019; Ding et al. 2021).

SN 2002ic is the first SN Ia found to show a strong ejecta–CSM interaction (Hamuy et al. 2003; Wang et al. 2004; Wood-Vasey et al. 2004). SN 2002ic-like SNe Ia are identified by a spectroscopic transition from Type Ia to Type II<sub>n</sub> after explosion. More such objects have been found (Aldering et al. 2006; Ofek et al. 2007; Taddia et al. 2012; Fox et al.

2015; Inerra et al. 2016). Further evidence of the presence of a significant amount CSM around SNe Ia came from spectroscopic observations of the narrow Na I D lines. Some SNe Ia show blueshifted and time-evolving narrow Na I D absorption lines (Patat et al. 2007; Blondin et al. 2009; Simon et al. 2009; Sternberg et al. 2011; Maguire et al. 2013; Wang et al. 2019). In particular, Wang et al. (2009) divided the spectroscopic normal SNe Ia into two groups: the normal-velocity ones and high-velocity ones, with Si II  $\lambda$ 6355 velocity lower or higher than 11,800 km s<sup>-1</sup> respectively. Wang et al. (2019) found that the SNe Ia with high-speed Si II features tend to be systematically associated with blueshifted Na I D lines. According to these studies, the distances of the CSM from the SNe range from 10<sup>15</sup> cm to 10<sup>19</sup> cm, and the mass loss rates that lead to such CSM are usually lower than 10<sup>-4</sup>–10<sup>-9</sup> M<sub>⊙</sub> yr<sup>-1</sup> if they are the results of steady stellar winds, consistent with the constraints set by X-ray and radio observations (Margutti et al. 2014; Pérez-Torres et al. 2014; Chomiuk et al. 2016; Lundqvist et al. 2020).

The presence of CSM can also alter the light curves and polarization of SNe Ia, due to light echoes caused by dust scattering (Chevalier 1986; Wang & Wheeler 1996; Patat 2005; Wang 2005; Goobar 2008; Ding et al. 2021). Light echoes from interstellar dust have been observed, such as the light echoes of SN 2006X (Crotts & Yourdon 2008; Wang et al. 2008a), SN 2014J (Crotts 2015; Yang et al. 2017), and some supernova remnants (Rest et al. 2008, 2012). Bulla et al. (2018) adopted a thin shell structure to fit the color evolution of several SNe Ia in the context of dust scattering, and suggested that the shells are typically located several parsecs away from the SNe. The result, however, as we will show in this study, is dependent on the assumed geometry of the dust distribution.

\* Supported by the National Natural Science Foundation of China.



Nagao et al. (2018) studied the polarization of SN 2012hn with two asymmetric CSM geometries (disk-like and jet-like), where the degree of polarization may be as large as a few percent. Although the high degree of polarization predicted in Nagao et al. (2018) is inconsistent with observations to date, such as those of SN 2005ke (Patat et al. 2012), 2009dc (Tanaka et al. 2010), and 2014J (Kawabata et al. 2014; Porter et al. 2016; Yang et al. 2018), it does provide a way of identifying the geometric distribution of CSM. Yang et al. (2018) obtained precise polarization images of SN 2014J from  $\sim 277$  days to  $\sim 1181$  days after the maximum light, and the polarization signal can be modeled by a dusty blob located around  $5 \times 10^{17}$  cm from the SN in the plane of the sky at the location of the SN.

Monte Carlo (MC) simulations can be used to solve the dust scattering process (e.g., Witt 1977; Gordon et al. 2001; Steinacker et al. 2013; Ding et al. 2021). One application of this method is to simulate the polarization in dusty galaxies by virtue of the dust scattering through the interstellar material (Bianchi et al. 1996; De Geyter et al. 2013; Peest et al. 2017). Another example is the scattering by the CSM around core-collapse supernovae, where light echoes and polarization signals are calculated by the MC method (Mauerhan et al. 2017; Nagao et al. 2017; Ding et al. 2021). The Henyey–Greenstein phase function is usually used as the formula for dust scattering (Henyey & Greenstein 1941). Other dust properties, such as the albedo, the cross section, and the asymmetry factor, can be taken from Draine (2003) and Draine & Lee (1984), assuming the dust properties are similar to those in either the Milky Way or the Large Magellanic Cloud.

A set of models are presented in this paper for the scattering by circumstellar dust of different geometric shapes around SNe Ia. Because there is strong evidence that the dust around SNe Ia may be systematically different from that in the Milky Way or the Large Magellanic Cloud (Wang et al. 2003; Patat et al. 2012; Wang et al. 2019), the dust properties are numerically calculated through Mie scattering theory for a given grain size distribution using the refractive index of Draine (2003). Section 2 describes the model, including the dust properties, the MC models, and the geometric distributions of the CSM. In Section 3, models are shown for a set of CSM distributions. Section 4 provides further discussions of the models and their applications to observational data. The conclusions are given in Section 5.

## 2. Models

### 2.1. Overview of the Radiative Transfer Process

Generally, the process of radiative transfer through the circumstellar (CS) dust includes scattering, absorption, and re-emission. The re-emission contributes to infrared flux and will not be considered here. The photon state in the Monte Carlo process is described by the Stokes parameters ( $S = (I, Q, U, V)^T$ ) following Chandrasekhar (1950), where  $I$  is the intensity,  $Q$  and  $U$  describe linear polarization,  $V$  describes circular polarization, and  $T$  stands for matrix transpose. The degree of linear polarization ( $P$ ) can be written as  $P = \sqrt{Q^2 + U^2}/I$ , in which the circular polarization ( $V$ ) is ignored in our models. Solving the radiative transfer process can be regarded as determining a kernel function that links the Stokes parameters

before and after the photon–CSM interaction:

$$S_\lambda(t', \Omega, \bar{U}) = S_{\lambda,0}(t') \exp(-\tau_\lambda) + \int I_{\lambda,0}(t' - t) K_{\lambda,S}(t, \Omega, \bar{U}) dt \quad (1)$$

where  $t'$  is the time after explosion,  $\Omega$  is the solid angle to the observer,  $S_{\lambda,0}(t')$  is the Stokes parameter at wavelength  $\lambda$  of the SNe Ia before dust scattering,  $\tau_\lambda$  is the optical depth at wavelength  $\lambda$ ,  $K_{\lambda,S}(t, \Omega, \bar{U})$  is a kernel function that can be calculated by assuming a  $\delta$ -function pulse as the input signal with  $\bar{U}$  being an array describing the parameters related to the geometric distribution and optical properties of the dust. Equation (1) contains two parts: the transmitted component along the line of sight  $S_{\lambda,0}(t') \exp(-\tau_\lambda)$ , and the scattered component  $\int I_{\lambda,0}(t' - t) K_{\lambda,S}(t, \Omega, \bar{U}) dt$ . We will use the optical depth in the  $B$  band as a measure of the optical properties of the CS dust. The optical depth of any given band can be directly calculated from that of the  $B$  band based on Mie scattering for a given dust distribution. The kernel function  $K_{\lambda,S}(t, \Omega, \bar{U})$  is a function of the dust properties, the scattering process, and the geometric distribution of CSM.

### 2.2. Dust Properties

In this study, all the values of albedo ( $\omega$ ), scattering cross section ( $\sigma_{\text{sca}}$ ), extinction cross section ( $\sigma_{\text{ext}}$ ), and scattering matrix are numerically calculated from Mie scattering theory (Wolf & Voshchinnikov 2004) based on the refractive index of dust grains from Draine (2003). The size distribution of the dust grains takes the following form:

$$f(r) = r^{-a_0} \exp \left\{ -b_0 \left( \log \frac{r}{r_0} \right)^{2.0} \right\} \quad (2)$$

where  $a_0$  and  $b_0$  are 4.0 and 7.5, respectively. The shape of the curve given in Equation (2) is consistent with the results in Nozawa et al. (2015), with  $r_0 = 0.05 \mu\text{m}$  representing the small size of dust grains with average radius of  $0.045 \mu\text{m}$ . The dust grains on the line of sight to SNe Ia are likely to be smaller than typical dust grains in the Milky Way, as may be inferred from the low values of the ratio of total to selective extinction for typical SNe Ia (Wang 2005; Wang et al. 2006; Foley et al. 2014; Amanullah et al. 2015; Gao et al. 2020). In addition, only silicate grains with single chemical composition are considered in our models; the difference is insignificant for models with both silicate and graphite grains (Gao et al. 2015).

### 2.3. Monte Carlo Method

The MC method includes several steps: the launching of photons, the tracking of photons through the CSM, and the integration of photons that have escaped from the CSM to build the kernel functions (Equation (1)) and solutions. Photons are launched with given Stokes parameters in a specific direction and propagate a certain distance until being absorbed or scattered. The photons are assumed to be unpolarized initially, as can be justified by spectropolarimetry of SNe Ia (Wang & Wheeler 2008), and their Stokes parameter is expressed as  $(1, 0, 0, 0)^T$ . The geometric size of the SN is much smaller than the extent of the scattering material and is thus set to zero in all the calculations. The radiation from the SN is assumed to be

spherically symmetric. The distance to the first photon–matter interaction depends on the optical depth in the radial direction, which is related to the composition and number density ( $N(R)$ ) of dust grains. Assuming a steady stellar wind with constant velocity, the density can be described by  $N(R) = A/R^2$  with  $A$  being a scaling parameter and  $R$  being the distance from the SN. The probability of a photon propagating a distance less than  $R_{\text{in}} + D$  without interacting with a dust particle is expressed as  $p(R < R_{\text{in}} + D) = 1 - \exp(-\tau(R_{\text{in}} + D))$ , where  $R_{\text{in}}$  is the inner boundary of the CSM and  $\tau(R_{\text{in}} + D)$  is the optical depth at the distance  $R_{\text{in}} + D$ . The probability  $p$  has a uniform distribution ranging from 0 to  $1 - \exp(-\tau_0)$ , where  $\tau_0$  is the optical depth of CSM in the direction of photon propagation. This treatment of the scattering process is identical to that of Witt (1977). Hence, the first free propagation distance  $D$  in the CSM could be generated through an MC process:

$$D = \frac{R_{\text{in}} A \sigma_{\text{ext}}}{A \sigma_{\text{ext}} + R_{\text{in}} \ln(\epsilon)} - R_{\text{in}} \quad (3)$$

where  $\epsilon$  is a random number in the range ( $\exp(-\tau_0)$ , 1). For scattering after the first interaction, we adopted the same approach as Witt (1977) by assuming a locally uniform distribution of CSM; the propagation distance of a photon is expressed as  $D = -\ln(\epsilon)/(N(R)\sigma_{\text{ext}})$ , with the range of the random number  $\epsilon$  being from 0 to 1.0.

The scattering process is calculated by computing the scattering angle following a distribution related to the scattering matrix and the Stokes parameters of the scattered photon by the rotational matrix and scattering matrix. To increase the computational efficiency, the absorption process is modeled by the weighting function as described in Witt (1977). Once the photon is out of the CSM, the Stokes parameters are integrated to the same arrival time at the observer inside a solid angle interval  $\Delta\Omega$ .

With the total number of photons ( $N_{\text{photon}}$ ) emitted in the MC program, the kernel function of the Stokes parameter is reconstructed as

$$K_{\lambda,S}(t, \Omega, \bar{U}) = (N_{\lambda,S}(t, \Omega, \bar{U})/N_{\text{photon}}) \times \Omega_{\text{emit}}/\Delta\Omega \quad (4)$$

where  $N_{\lambda,S}(t, \Omega, \bar{U})$  is the corresponding values of the Stokes parameter with a time delay  $t$  and integrated over the solid angle  $\Delta\Omega$ . The size of  $\Delta\Omega$  determines the angular resolution of the model,  $N_{\text{photon}}$  is the total number of injected photons in the calculations,  $\Omega_{\text{emit}}$  is the solid angle in which the photons are injected into the CSM, and  $\Delta\Omega$  is the solid angle over which the photons escaping from the CSM are integrated. For a spherically symmetric structure, the solid angles of both emitted and collected photons ( $\Omega_{\text{emit}}$  and  $\Delta\Omega$ ) are  $4\pi$ . For an axially symmetric disk or axisymmetric shell  $\Delta\Omega$  is  $2\pi \sin\theta\Delta\theta$ , where  $\Delta\theta$  is the opening angle from the line of sight and is equal to  $1^\circ$  in our model to ensure the accuracy of light curves and polarization. For convenience, the kernel function  $K_{\lambda,S}(t, \Omega, \bar{U})$  is simplified to  $K_S(t)$ .  $K_I(t)$ ,  $K_Q(t)$ , and  $K_U(t)$  represent the kernel functions of Stokes parameters  $I$ ,  $Q$ , and  $U$ , respectively. With all the reconstruction above, it is clear that  $K_I = 1$  if there is no CSM-induced polarization.

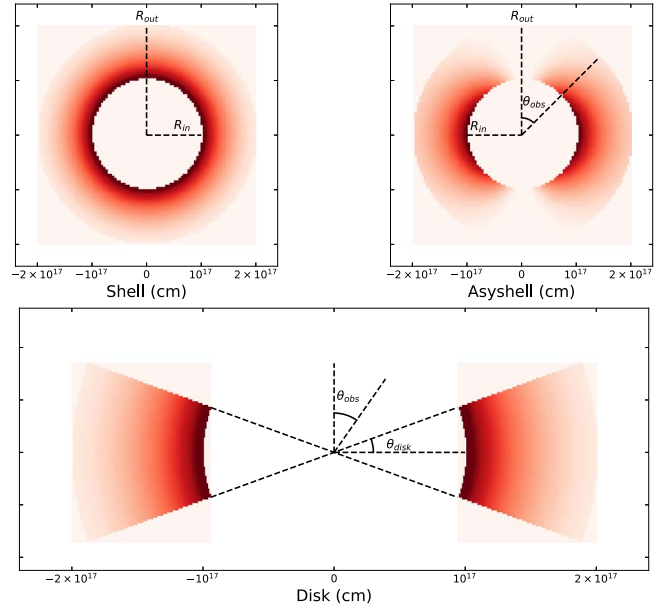


**Figure 1.** Three types of CSM distributions: spherical shell (top left), axisymmetric shell (Asyshell, top right), and axisymmetric disk (bottom). The transparency of the color represents the number density of dust grains.

#### 2.4. Geometric Distributions of CSM

We considered three different geometric distributions of the CSM. These are spherical shells, axisymmetric disks, and axisymmetric shells—as shown in Figure 1, which is similar to the plot in Figure 3 of Wang et al. (2019). The shell or disk structures may arise from the stellar wind or accretion/excretion disks of the progenitor systems of SNe Ia. The details of the geometric structure are not known but it is nonspherical, which can be expected based on observations of the stellar environment around known white dwarfs; the geometry carries important information in understanding the mass loss history of the progenitor systems.

With Figure 1 we can define the model parameters for the calculations of dust scattering. These are the inner ( $R_{\text{in}}$ ) and outer ( $R_{\text{out}}$ ) radii that define the boundaries of the dust distribution; from them we define the extent of the CSM as  $R_{\text{wid}} = R_{\text{out}} - R_{\text{in}}$ . As shown in Figure 1, the angle to the observer is given by  $\theta_{\text{obs}}$ , and the opening angle of the disk is  $\theta_{\text{disk}}$ . For the shell and disk structures, the number density of dust grains in the radial direction is given as  $A/R^2$ , where the parameter  $A$  is a scaling constant and  $R$  is the distance to the SN. For the axisymmetric shell structure, the density follows the relation  $N(R, \theta) = (A/R^2) \times (s_0 |\sin\theta|^m + 1 - s_0)$ , where parameters  $m$  and  $s_0$  capture the level of angular asymmetries.  $s_0 = 0$  indicates that the axisymmetric shell is reduced to a spherical shell, and the range of  $s_0$  is from 0 to 1. The parameter  $m > 0$  represents the degree of dust-gathering in the direction of the equator. With the definition of the number density of dust grains  $N(R)$ , the optical depth  $\tau$  in the radial direction is expressed as  $\int N(R)\sigma_{\text{ext}}dR$ . Thus, three parameters ( $R_{\text{in}}$ ,  $R_{\text{wid}}$ ,  $\tau$ ) are needed to define the geometric properties of a spherical shell. Four parameters are needed for an axisymmetric disk: ( $R_{\text{in}}$ ,  $R_{\text{wid}}$ ,  $\tau$ ,  $\theta_{\text{disk}}$ ). Five parameters are needed for an axisymmetric shell: ( $R_{\text{in}}$ ,  $R_{\text{wid}}$ ,  $\tau$ ,  $m$ ,  $s_0$ ). Notice that the optical depth of the axisymmetric shell is defined in the direction with the maximum number density of dust grains. The

**Table 1**  
CSM Parameter Ranges and Numbers of Grids of the Three Structures

	Parameter Range	Numbers of Grids	
$R_{\text{in}}$	[20, 200]	19	S, D, A
$R_{\text{wid}}$	[20, 200]	19	S, D, A
$\tau$	[0.1, 1.0]	10	D
$\tau$	[0.05, 0.25]	5	S, A
$\theta_{\text{disk}}$	[6°, 30°]	5	D
$(m, s_0)$	[(0.5, 0.1), (5.0, 1.0)]	10	A
$\theta_{\text{obs}}$	[10°, 90°]	9	D, A

**Note.** The grids are uniformly distributed in the parameter ranges. The labels ‘‘S,’’ ‘‘D,’’ and ‘‘A’’ represent the spherical shell, axisymmetric disk, and axisymmetric shell, respectively. Here,  $R_{\text{in}}$  and  $R_{\text{wid}}$  are measured in light-days.

angle to the observer  $\theta_{\text{obs}}$  is needed as an additional parameter for the axisymmetric shell and disk structures.

The likely values for the parameters are poorly known. An SN 2002ic-like supernova represents an extreme case where the progenitor has lost a rather large amount of matter shortly before the SN explosion (Hamuy et al. 2003; Wang et al. 2004; Aldering et al. 2006). Spectropolarimetry shows that the interaction between the SN ejecta and the CSM is highly asymmetric (Wang et al. 2004). In the recurrent nova scenario developed by Moore & Bildsten (2012) for these supernovae, a diffusing medium-velocity ( $\sim 10\text{--}100 \text{ km s}^{-1}$ ) CSM was ejected shortly before the supernova explosions. Spectroscopically normal SNe Ia may have CSM at significantly larger distances but this has so far escaped any observational detection. In this study, the dusty CSM is restricted to being at distances around  $10^{17}$  cm following the work of Wang et al. (2019).

### 3. Results

#### 3.1. Kernel of Intensity

The kernel function  $K_I(t)$  is the distribution of scattered photons as a function of the delay time  $t$  for a  $\delta$ -function impulse of input light. This distribution is affected by physical properties of the CSM and its geometry. However, a variety of CSM parameters may produce very similar kernel functions  $K_I(t)$  and this introduces a considerable amount of degeneracy, which makes it difficult to disentangle the various effects involved. For an axisymmetric disk or shell, observers at smaller  $\theta_{\text{obs}}$  will detect a broader range of time delays, similar to the effect caused by a larger  $R_{\text{in}}$ . Larger  $\theta_{\text{disk}}$  for an axisymmetric disk, smaller  $(m, s_0)$  for an axisymmetric shell, and larger values of  $\tau$  all lead to a larger number of scattered photons.

To understand such degeneracy, we calculated the kernel functions for parameter grids that cover a broad range of the geometric distribution of the CSM. Table 1 shows the configuration of the CSM parameter grids. The total number of parameter grids is 1805 ( $19 \times 19 \times 5$ ) for the spherical shell, and 18,050 ( $19 \times 19 \times 5 \times 10$ ) for the axisymmetric disk and axisymmetric shell models. For each simulation of the axisymmetric disk or axisymmetric shell, nine observing angles uniformly distributed from 10° to 90° were calculated. The degeneracy of CSM parameters is complicated. For illustrative purposes only, we defined three reference sets of CSM parameters S1, D1, and A1 for the spherical shell,

**Table 2**  
Chosen CSM Parameters of the Shell (S), Disk (D), and Axisymmetric Shell (A) Structures

	$R_{\text{in}}$ (lt-day)	$R_{\text{wid}}$ (lt-day)	$\tau$	$\theta_{\text{disk}}$	$(m, s_0)$	$\theta_{\text{obs}}$
S1	40	40	0.15			
S2	50	20	0.15			
S3	20	140	0.2			
D1	40	40	0.5	18°		30°
D2	20	150	0.7	12°		10°
D3	30	70	0.3	24°		20°
D4	140	20	0.8	24°		60°
D5	140	110	0.9	30°		90°
A1	40	40	0.15		(2.5, 0.5)	30°
A2	20	120	0.25		(4.5, 0.9)	10°
A3	30	90	0.15		(0.5, 0.1)	90°
A4	40	30	0.2		(3.5, 0.7)	90°

**Note.** S1, D1, and A1 are the corresponding reference CSM parameters. The unit lt-day denotes light-day.

axisymmetric disk, and axisymmetric shell, respectively, to examine the parameter degeneracy. The parameters that define reference sets are shown in Table 2. The CSM parameters of these characteristic sets are consistent with the fitting results in Wang et al. (2019) and Li et al. (2019), where the likely distances from the CSM around a few high-velocity SNe Ia were found to be approximately  $(1\text{--}2) \times 10^{17}$  cm. The optical depths were found to be around 0.7 for the axisymmetric disk model and 0.15 for the spherical shell and axisymmetric shell models.

Scattered light close to the optical maximum is mixed with the bright SN light and is hard to detect photometrically. Late-time data are more useful in quantitative diagnostics of the circumstellar dust. The degeneracy of the kernel function after maximum light can be evaluated quantitatively by defining two measures: the average of  $K_I(t)$  from 20 days to 100 days  $K_{I\text{mean}} = \sum_{i=20}^{100} K_I(i)/81$ , and the ratio of the intensities at 100 days and 20 days  $K_{I\text{ratio}} = K_I(100)/K_I(20)$ . The similarity of the kernel function  $K_I(t)$  is defined by the following criteria:  $|K_{I\text{mean}} - K_{I\text{mean}}^0|/K_{I\text{mean}}^0 < 0.1$  and  $|K_{I\text{ratio}} - K_{I\text{ratio}}^0|/K_{I\text{ratio}}^0 < 0.1$ , where  $K_{I\text{mean}}^0$  and  $K_{I\text{ratio}}^0$  correspond to the values for the reference model S1, D1, or A1.

With the above criteria, seven sets of spherical shell models share similar late-time kernel distributions to the reference model S1, while for the reference cases D1 and A1, 881 and 564 sets show similar late-time kernel functions, respectively. For the three geometric models of the CSM, the fraction of late-time kernel functions that are similar to their corresponding reference models is less than 1% of the total number of models. Figure 2 shows all of the kernel functions similar to S1 at late time for the spherical shell model in the top panel and 100 models randomly selected from similar models for the axisymmetric disk and axisymmetric shell models (middle and bottom panels). For comparison, several characteristic cases are highlighted for the spherical shell model (S1, S2, and S3), axisymmetric disk model (D1, D2, D3, D4, and D5), and axisymmetric shell (A1, A2, A3, and A4). The individual CSM parameters for these characteristic cases are listed in Table 2. The degeneracy is obvious; e.g., for the axisymmetric shell model, the large  $\tau$  and  $(m, s_0)$  values in case A2 and the small corresponding values in case A3 result in a similar kernel function  $K_I(t)$ . As we just discussed, with this kernel function

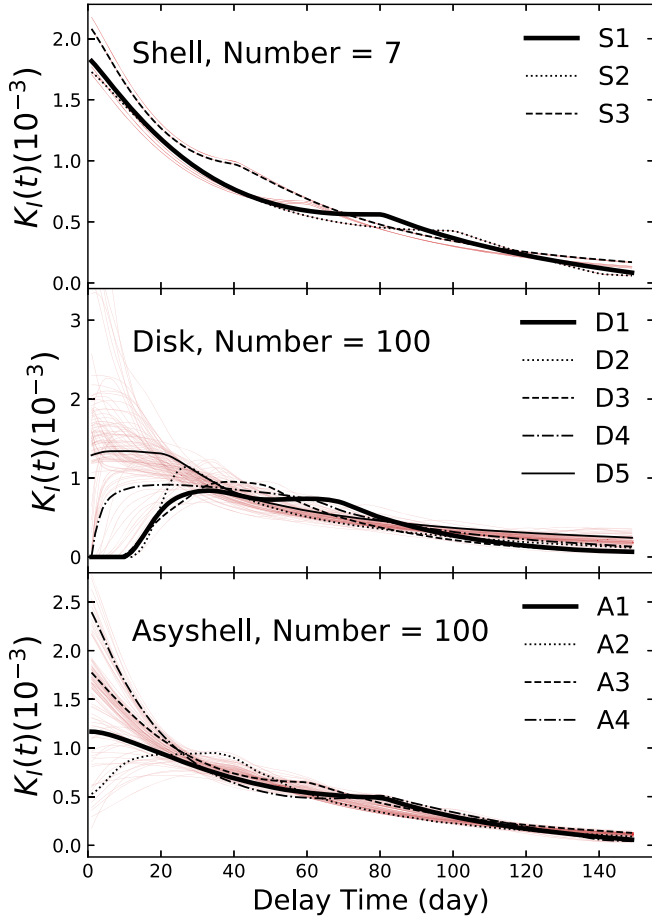


**Figure 2.** Upper panel: kernel functions  $K_I(t)$  that are similar to the reference case S1 for the spherical shell model. The black solid, dotted, and dashed lines are for models S1, S2, and S3, respectively. The other similar models are shown as thin red lines. Middle panel: kernel functions that are similar to the reference case D1. The black thick solid, dotted, dashed, dashed-dotted, and thin solid lines show models D1, D2, D3, D4, and D5. The red lines show 100 models randomly chosen from the 881  $K_I(t)$  models that are similar to D1. Lower panel: kernel functions that are similar to the reference case A1. The black thick solid, dotted, dashed, and dashed-dotted lines show models A1, A2, A3, and A4, respectively. The thin red lines show 100 models randomly selected from the 564  $K_I(t)$  models that are similar to D1. The details of the models shown in black lines can be found in Table 2.

degeneracy, the CSM parameters cannot be determined by fitting the light-curve data only.

### 3.2. Kernel of the Stokes Parameter $Q$

Polarization can be a powerful diagnostic tool if dust scattering is indeed important. For the spherical shell, the polarization of the scattered photons cancels out, and there would be no net polarization. On the other hand, the scattered light from the axisymmetric disk or axisymmetric shell may be highly polarized. Without loss of generality, we will assume that the axis of symmetry of the disk is pointing north, the Stokes parameter  $U$  of the axisymmetric disk and axisymmetric shell is zero, and only the Stokes parameter  $Q$  is nonzero, with the degree of polarization  $P = |Q|/I$ .

The degree of polarization is most significant when the target is viewed edge-on ( $\theta_{\text{obs}} = 90^\circ$ ), and is zero when it is viewed face-on ( $\theta_{\text{obs}} = 0^\circ$ ). In addition to the geometric distribution, polarization also depends on the optical cross section and albedo of the dust grains. Again, the polarization can be

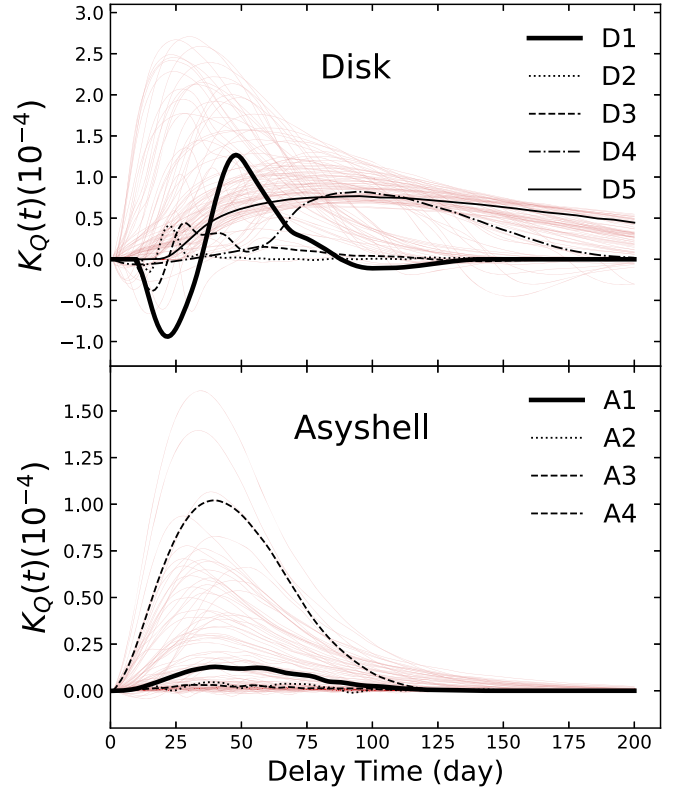


**Figure 3.** Same as Figure 2, but for the kernel function of Stokes parameter  $Q$  just for the disk model (upper panel) and axisymmetric shell model (lower panel). They have the same CSM parameters as the 100 randomly selected cases for both models.

calculated by first calculating the kernel function  $K_Q(t)$  for the Stokes parameter  $Q$ , by assuming the light source is a  $\delta$ -function.

The different CSM parameters that generate very similar kernel functions of the intensity (Figure 2) now generate dramatically different kernel functions for the Stokes parameter  $Q$ . This demonstrates that the combination of  $K_I(t)$  and  $K_Q(t)$  can distinguish the different dust geometries and thus break the degeneracy. Figure 3 shows the kernel function  $K_Q(t)$  of the 100 cases shown in Figure 2 for the axisymmetric disk and axisymmetric shell models. The polarization curves show a broad range of behaviors, which makes them very powerful in establishing the presence of CS dust and constraining their geometric structures. As an example,  $K_Q(t)$  of D3 is smaller than that of D5 owing to a smaller  $\theta_{\text{obs}}$ , and the time evolution of the degree of polarization is sensitive to the geometric size and location of the dust. With the same  $\theta_{\text{obs}}$  of  $90^\circ$ , A3 and A4 have distinctively different  $K_Q(t)$  owing to their different values of  $(m, s_0)$ .

### 3.3. $Q - U$ Distribution for Reference Cases D1 and A1

Light echoes can be used as a tomographic method that can effectively probe the 3D geometry of the scattering material. This tool becomes even more powerful with the inclusion of polarimetry. It is interesting to note that the two models D1 and A1 have very different  $K_Q(t)$  curves, but with geometric structures that are rather similar (Figure 3). The differences can be examined by calculating the surface brightness of the scattered light and the 2D  $Q - U$  distributions for the reference cases A1 and D1. For the purpose of making the figures, we

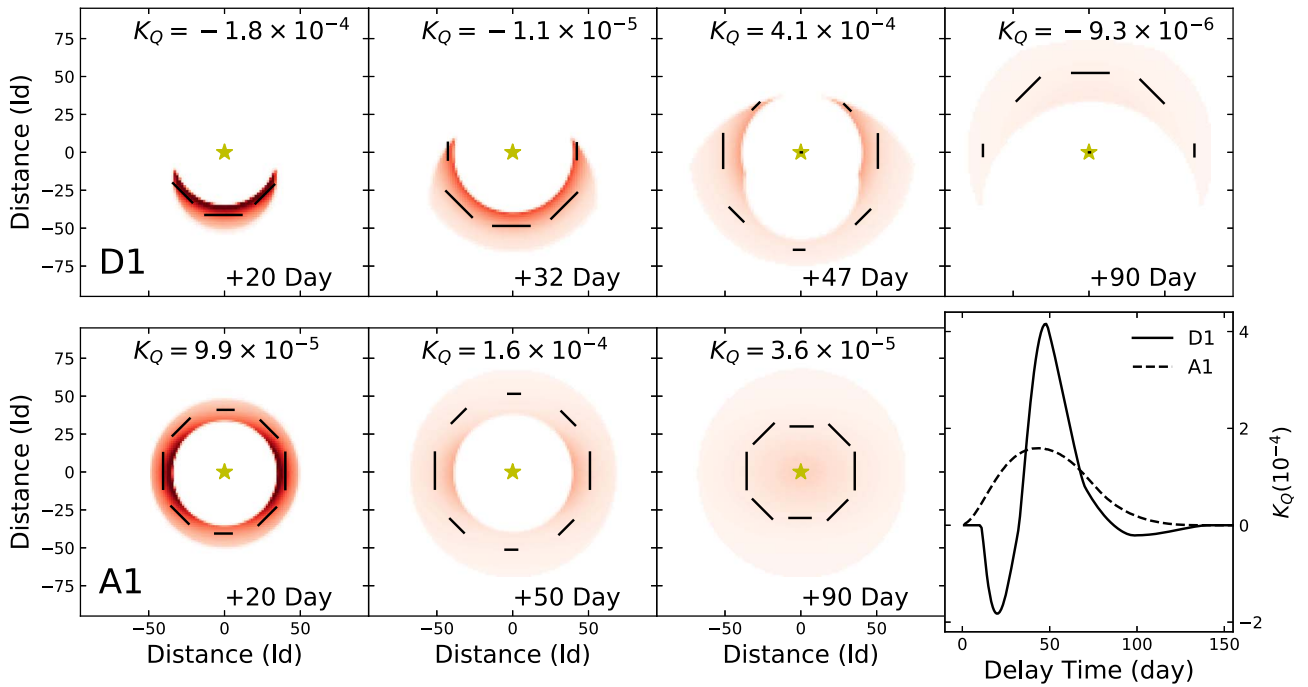


**Figure 4.** Upper panels: the intersecting area between the parabolic surface and the CSM projecting to the line of sight (red region) and  $Q - U$  vectors (short black lines) of four epochs (+20 days, +32 days, +47 days, and +90 days) for the disk model D1. Lower panels: three epochs (+20 days, +50 days, and +90 days) for the axisymmetric shell model A1; far right lower panel: the corresponding  $K_Q(t)$  curves of the disk and axisymmetric shell models. The observing angle  $\theta_{\text{obs}}$  for both models A1 and D1 is  $30^\circ$  and the other parameter values are shown in Table 2.

assumed the single-scattering approximation. The results are shown in Figure 4.

The axisymmetry ensures that the integrated Stokes parameter  $U$  is 0, therefore only the  $Q$  component of the Stokes parameter needs to be considered. For the axisymmetric shell structure,  $Q$  from the equatorial region is always larger than  $Q$  from the two polar directions. Thus,  $K_Q(t)$  is positive with any  $\theta_{\text{obs}}$  or any values of CSM parameters for the axisymmetric shell model A1. This means that  $K_Q(t)$  never changes sign, as shown in the bottom panel of Figure 3. For the disk model, the polarization may be dominated by scattering from either the equatorial or the polar regions depending on the epoch of observations. This causes  $K_Q(t)$  to change sign with time, as shown in Figures 3 and 4. Note that the degrees of polarization are slightly different in Figures 3 and 4 for models D1 and A1. This is because multiple scattering is assumed in Figure 3 but the single-scattering approximation is assumed in Figure 4 for illustrative purposes.

#### 4. The Scattered Light of Type Ia Supernovae

In this section, the kernel functions are convolved with a spectral energy distribution (SED) template to predict the light curves, polarization, and spectral evolution of Type Ia supernovae. We will also apply these models to fit the  $E(B - V)$  color curves, as has been done previously in Bulla et al. (2018), but with the goal of studying the degenerate nature of the model parameters and the difficulties in uniquely constraining the CS dust geometry without a detailed time sequence of polarimetry.

##### 4.1. The Light Curves and Polarization

The template for light curves or spectra should come from SNe Ia without CS dust in their vicinity. Here, the spectral

template is adopted from Hsiao et al. (2007). This template is used to derive the light curves by applying the filter transmission functions. Figure 5 shows the  $B$ -band light curves and polarizations for the dust models we have investigated, obtained by convolving the spectral template with the relevant kernel functions derived in the previous section. A common feature of the models with CS dust scattering is a flux excess a month or so after the maximum brightness.

As a consequence of the sensitivity of the kernel function  $K_Q(t)$  to the dust distribution geometry, the predicted polarization curves are dramatically different for different model parameters. This makes polarimetry a promising tool for constraining the dust distribution around SNe Ia. We note that the majority of disk models predict large degrees of polarization that are observable for nearby supernovae. For the parameters we have adopted, the axisymmetric shells predict degrees of polarization that are in general lower than 1.0%. In both the axisymmetric shell and disk cases, the degree of polarization peaks at around 50 days past optical maximum, and for the axisymmetric disk model the degree of polarization can be as large as a few percent. A time sequence of polarimetry at  $\sim 2$  months can be used to test these models and establish or disprove the existence of CS dust around SNe Ia. No polarization evolution at such late phases has been acquired for any SN Ia so far.

##### 4.2. Constraining the Distance from Multiple-epoch Polarization

The results above suggest that the combined observation of the photometry and polarization is a promising probe for constraining CSM features, which is based on the results that similar light curves may be related to a variety of CSM parameters while the corresponding polarization curves may help to break this degeneracy. In this section, we show that

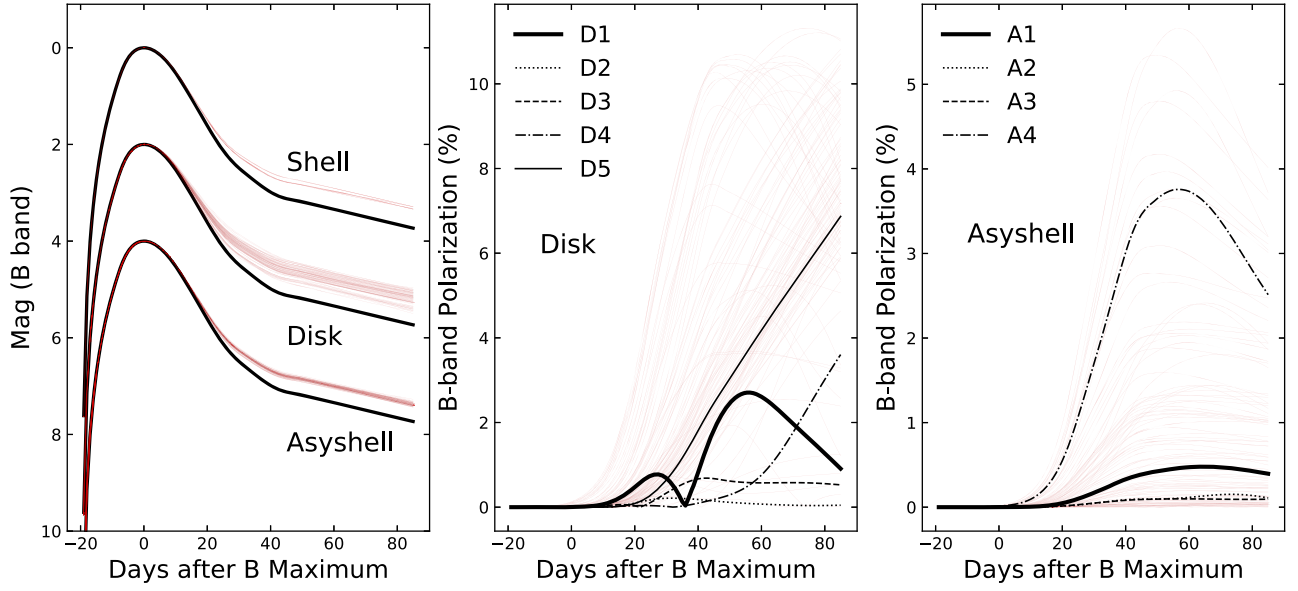


**Figure 5.** Left panel: the predicted B-band light curves (red lines) with the same CSM parameter values as in Figure 2 vs. the B-band template of SNe Ia (black lines). All the light curves are scaled to their maximum light. Middle and right panels: the predicted polarization curves of a disk and an axisymmetric shell, respectively.

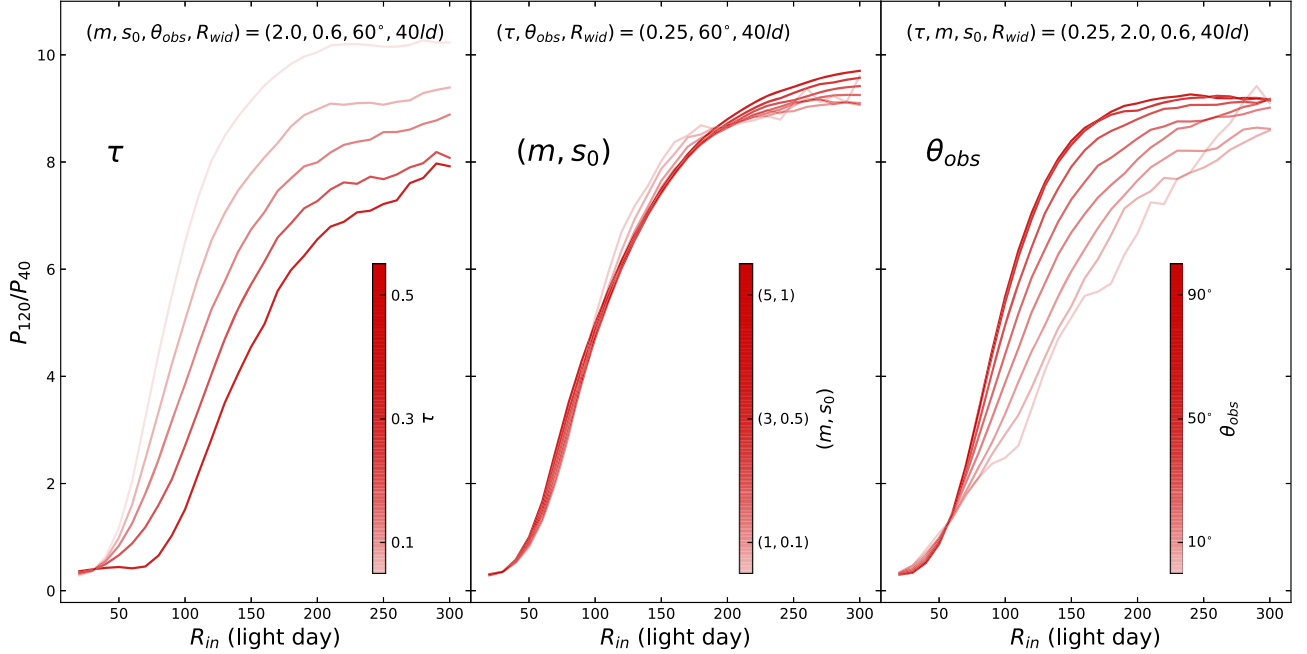


**Figure 6.** The polarization ratio  $P_{120}/P_{40}$  is approximately a monotonic function of  $R_{in}$  as shown in each panel. The depth of color represents the changing values of parameter  $\tau$  (left panel),  $(m, s_0)$  (middle panel), and  $\theta_{obs}$  (right panel). For each configuration, the thickness of the CS dust in the radial direction  $R_{wid}$  is set to 40 lt-day. For each panel, the values of the other relevant parameters are shown at the top.

polarimetry is a crucial probe for constraining the CSM around SNe Ia.

Take the axisymmetric shell models as examples: the degree of polarization is sensitive to  $\tau$ ,  $(m, s_0)$ , and  $\theta_{obs}$ . The values of these four parameters affect the overall levels of polarization. On the other hand, the inner or outer boundaries of CSM are sensitive to the time evolution of the degree of polarization. These properties can be employed to constrain the location of the CS dust.

In order to quantify the effect of the CSM boundary on the degree of polarization, we calculated the ratio of the degrees of polarization at +120 and +40 days,  $P_{120}/P_{40}$ . If the distance of CSM is significantly smaller than 40 lt-day ( $\sim 1 \times 10^{17}$  cm),

the typical delay time of scattered photons is small and the degree of polarization at +40 days is usually larger than that at +120 days. But if the distance of CSM is mostly around 120 lt-day ( $\sim 3 \times 10^{17}$  cm), the polarization ratio may just be the opposite.

Figure 6 shows the relationship between the polarization ratio  $P_{120}/P_{40}$  and the inner boundary of CSM. It can be clearly seen that for different values of  $\tau$ ,  $(m, s_0)$ , and  $\theta_{obs}$ , an approximately monotonic relationship can be established between the polarization ratio  $P_{120}/P_{40}$  and the location of the inner boundary  $R_{in}$ . For the polarization ratio shown in Figure 6,  $R_{wid}$  is set to 40 lt-day in all simulations. As expected, Figure 6 shows also that the polarization ratio can be dependent

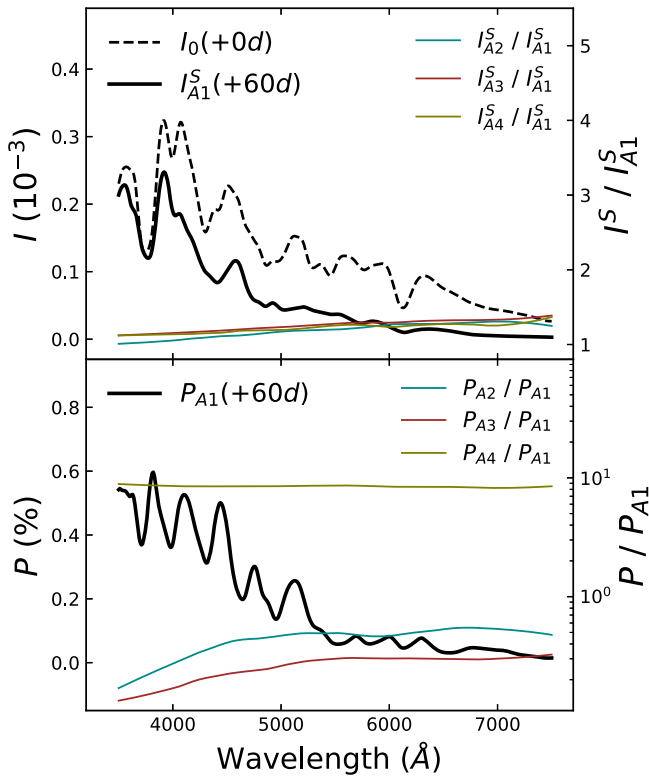


**Figure 7.** Upper panel: the dashed black line shows the spectral template ( $I_0$ ) of SNe Ia at maximum light reduced to an arbitrary scale for clarity. The black line shows the scattered spectrum of the CSM model A1 at +60 days after peak brightness. The three colored solid lines show the ratios of the scattered intensities ( $I^S/I_{A1}^S$ ) of the CSM models A2, A3, and A4 and model A1. Lower panel: the black line is the polarization spectrum of the CSM model A1. The three colored solid lines are the ratios of the polarizations ( $P/P_{A1}$ ) of the CSM models A2, A3, or A4 and the model A1. The values of the CSM parameters of A1, A2, A3, and A4 are listed in Table 2.

on the optical depth and the direction of the observations, but the sensitivity relative to the parameters describing the level of asymmetry is rather weak.

#### 4.3. The Spectra of Type Ia Supernovae with an Axisymmetric Dusty Circumstellar Shell

The spectroscopic and spectropolarimetric evolution of SNe Ia can be affected by the presence of asymmetric dusty CSM. As an example, Figure 7 shows the spectrum of the scattered light and the corresponding spectropolarimetry at day 60 after optical maximum of a typical SN Ia, for the parameter sets A1, A2, A3, and A4 (see Table 1 for details). In the top panel, we show a spectrum of the scattered light at day 60 for the reference case A1 (black solid line), which is quite similar to the adopted spectral template (black dashed line) at optical maximum. This similarity suggests the scattered photons are dominated by those from the peak brightness. Among the models we have explored, the CS dust geometry has only a weak effect on the spectral features of the scattered light. For example, the ratios of scattered spectra of A2, A3, and A4 to that of the reference case A1, shown as the colored lines in Figure 7, exhibit no strong spectral modulation in the wavelength range from 350 to 750 nm. Similar behavior can be seen in the degree of polarization shown in the bottom panel, although the degrees of polarization are significantly different for different models. In general, the fitting of

spectropolarimetry can place tighter constraints on the dust properties, such as the chemical composition and the size distribution of the dust grains, but a time sequence of broadband polarimetry is sufficient to constrain the geometric shape of the CS dust. Densely time-sampled spectropolarimetry (e.g., more than two observations in late phases) can be difficult when considering observational cost but is fortunately not needed.

#### 4.4. The $E(B - V)$ Curves of SN 2006X and SN 2014J and Their CS Dust

SN 2006X (Wang et al. 2008b) and SN 2014J (Marion et al. 2015; Srivastav et al. 2016; Yang et al. 2017) are two highly reddened nearby supernovae. They can serve as good examples to study the location of dust along the lines of sight to the SNe.

Dust scattering is color-sensitive and, if present, can alter the evolution of the color excess  $E(B - V)$ . Bulla et al. (2018) adopt a thin shell geometry for the CS or interstellar dust to model the color excess  $E(B - V)$  curves of SNe Ia to place constraints on the location of the dust. A single spherical shell is used to simultaneously fit the large values of  $E(B - V)$  and its time evolution. Therefore, the optical depth of the shell is fixed by the total reddening. In their models, the radius of the inner boundary is set to 0.95 times of the radius of the outer boundary. The dust distribution is uniform in the shell. Their models assume the Henyey–Greenstein dust scattering phase function (Henyey & Greenstein 1941) and Milky Way-like dust grains. The radii of the dusty shells for SN 2006X and SN 2014J are found to be 44.6 pc (or  $\sim 10^{20}$  cm) and 17.3 pc (or  $\sim 5 \times 10^{19}$  cm), respectively, according to these models, thus placing the dust grains at distances that are typically beyond those for CSM. These distances are also much larger than the distances of the putative CSM derived by Wang et al. (2019) based on the evolution of the narrow Na I D lines.

In reality, the distribution of the dust responsible for the heavily reddened SNe such as SN 2006X and SN 2014J may be rather complicated. The extinction may come from the interstellar dust across the host galaxy along the line of sight (e.g., the spiral arm area), the dusty interstellar environment close to SNe Ia (e.g., a few parsecs as shown in Bulla et al. 2018), or from CS dust. In this paper, we assume that the extinction of highly reddening SNe 2006X and 2014J comes from the interstellar dust across the host galaxy and the CS dust around SNe Ia. Thus, the interstellar dust is less likely to be the cause of time-varying reddening, and only the time evolution of  $E(B - V)$  may likely reveal the CS dust. Both the scenarios shown in Bulla et al. (2018) and in our work can explain the time evolution of  $E(B - V)$  reasonably, but polarimetry (as discussed in our work) and thermal emission from dust in the CSM are efficient probes to distinguish them.

As we have shown already, there is a considerable amount of degeneracy among the model parameters. To compare with the results of Bulla et al. (2018), we consider the simple spherical shell model at three distances of  $\sim 10^{17}$  cm,  $\sim 10^{18}$  cm, and  $\sim 10^{19}$  cm to fit the  $E(B - V)$  color curves of SN 2006X and 2014J. For SN 2006X, the optical depths are 0.3, 2.1, and 4.8 for the shells at the distances of  $10^{17}$  cm,  $10^{18}$  cm, and  $10^{19}$  cm, respectively. For SN 2014J, the optical depths are 0.12, 0.97, and 1.5 at these three distances. The source of the observed  $E(B - V)$  curves is the compilations of Bulla et al. (2018), and the original sources of the data are Wang et al. (2008b) for SN 2006X and Amanullah et al. (2015) for SN 2014J. The

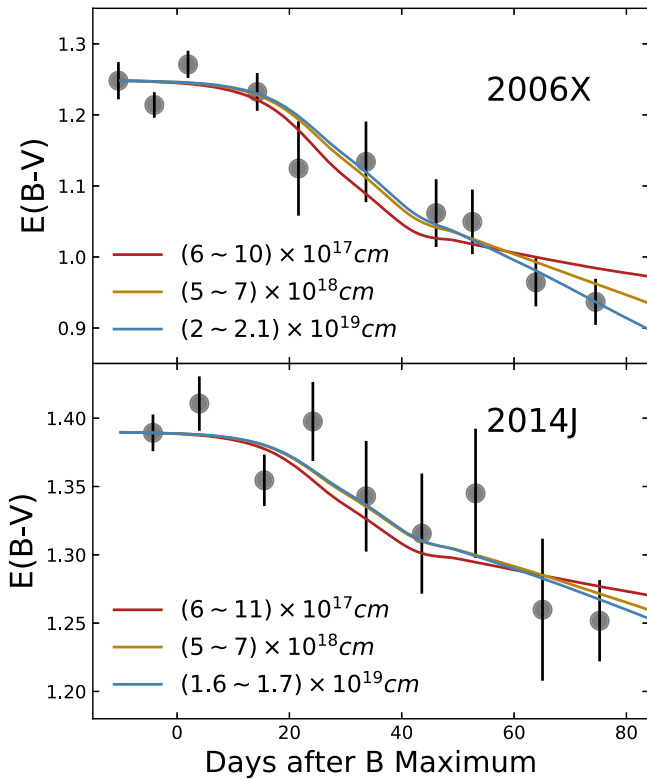


**Figure 8.** The circles are the data of  $E(B - V)$  curves of SN 2006X (top panel) and SN 2014J (bottom panel) from Bulla et al. (2018). The three lines in each panel represent three shell models with different distances from the center, and they have been shifted to match  $E(B - V)$  along the line of sight for SN 2006X and SN 2014J. This shows that the color curves alone cannot provide strong constraints on the location of the CS dust.

results are shown in Figure 8. All three shell models can fit the time evolution of  $E(B - V)$  satisfactorily, confirming the degenerate nature of model parameters. A similar result could be acquired in the opposite way of fitting the CSM distance by fixing the optical depth  $\tau$ . For instance, if we fix  $\tau$  with the values of 0.3, 2.0, and 5.0, the corresponding values of  $R_{\text{in}}$  for SN 2006X would be about  $10^{17}$  cm,  $10^{18}$  cm, and  $10^{19}$  cm by fitting its photometric data. Meanwhile, our result is consistent with that in Bulla et al. (2018) if we fix  $\tau$  with some relatively large value. For instance, the shell distance for SN 2014J in Bulla et al. (2018) is about  $5 \times 10^{19}$  cm, while the distance in our work is around  $1.6 \times 10^{19}$  cm. These two results are consistent with each other. The slight difference might be due to the dust properties, the scattering process, or the choice of the template of the light curve adopted in our models. We thus point out that even well observed photometric data of highly extinct SNe may not be sufficient to constrain the location of the dust in the context of light echo models. Multiepoch image polarimetry is an important complementary probe to reveal the location of dust in CSM.

#### 4.5. Fitting the Distance of CSM around SN 2014J through Polarization

On the one hand, the interstellar dust produces polarization through dichroic absorption, which is unlikely to show strong time evolution. On the other hand, in the scenario where the late-phase light curve of SNe Ia includes the scattered light from interstellar dust, the scattering angle should be as small as about  $5^\circ$ , constrained by the delay time (e.g.,  $\sim 50$  days) and the

**Table 3**  
Parameter Values of Asyshell1, Asyshell2, and Asyshell3 Models Shown in Figure 9

	$\tau$	$R_{\text{in}}$ (lt-day)	$R_{\text{wid}}$ (lt-day)	$m$	$s_0$	$\theta_{\text{obs}}$
Asyshell1	0.16	35	50	2.0	0.9	$70^\circ$
Asyshell2	0.24	140	140	3.0	0.5	$30^\circ$
Asyshell3	0.35	200	40	3.5	0.7	$40^\circ$

distance of interstellar dust (e.g.,  $\sim 10$  pc). Such a small scattering angle cannot introduce significant polarization signals. Thus, we show that the time evolution of the polarization is a deterministic signature of CS dust polarization. However, there are few late-phase polarimetries (e.g., 100 days after peak light, and see references such as Cikota et al. 2019; Chu et al. 2022) on SNe Ia due to the time-consuming observations. SN 2014J is one that has been observed by imaging polarimetry during such a late phase, and this provides an excellent opportunity to constrain the parameter values of CSM. As reported by Yang et al. (2018), the image polarimetry shows an apparent deviation of about 1.0% in the  $F475W$  band of the Hubble Space Telescope (HST) at around +277 days after maximum light compared to the polarization at the peak brightness. This deviation is highly possible from the scattering effect of CS dust instead of interstellar dust. Yang et al. (2018) attributed these polarization signals to the scattering from a dusty cloud located at around  $5 \times 10^{17}$  cm from the SN. Here we apply our CS dust scattering model to study the photometry and polarimetry of SN 2014J.

The models are constructed for the axisymmetric shell geometry. The models Asyshell2 and Asyshell3 are two sets of axisymmetric shells that can fit the photometric and polarimetric data of SN 2014J reasonably. The model parameters are shown in Table 3. The model fits to the  $B$ -band light curve and the polarizations are shown in Figure 9. The location of the CS dust is at distances larger than 140 lt-day (Table 3). For comparison, an axisymmetric shell with relatively close distance (Asyshell1) is also displayed, which can fit the light curves and the polarization signal up to 277 days after maximum light precisely, but is excluded by the lack of a clear evolution in the degree of polarization at early times (Kawabata et al. 2014; Yang et al. 2018).

Obviously, the value of  $P_{120}/P_{40}$  is less than 1.0 for Asyshell1 and is much larger than 1.0 for both Asyshell2 and Asyshell3 models. Determining whether Asyshell2 or Asyshell3 is more reasonable for the potential distribution of CSM around SN 2014J is slightly ambiguous. Figure 9 shows that Asyshell2 produces relatively small degrees of polarization at all epochs and Asyshell3 produces large polarization about 200 days after  $B$ -band maximum light, though there are no observations on the polarization at the same epochs. Nevertheless, the distance of CSM around SN 2014J is about  $5 \times 10^{17}$  cm, which is consistent with the results in Yang et al. (2018), though two different distributions (the axisymmetric shell and blob) are used respectively. The mass loss rate of the stellar wind is about  $5 \times 10^{-6} M_\odot \text{yr}^{-1}$  for model Asyshell2, which is consistent with the observational restrictions on CSM and the progenitor of SN 2014J from  $H\alpha$ , infrared, and X-ray signals (Margutti et al. 2014; Lundqvist et al. 2015; Sand et al. 2016; Johansson et al. 2017).

Yang et al. (2018) also acquired the broadband polarization of SN 2014J for 277 days after maximum light in HST  $F606W$

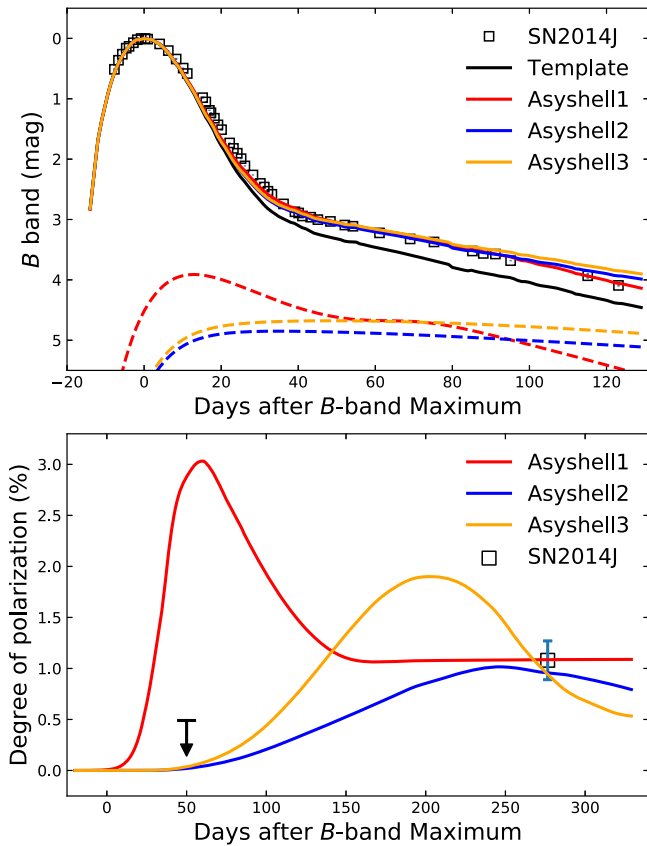


**Figure 9.** In the upper panel, the black line is the template of  $B$ -band light curve. The red, blue, and orange solid lines are the fitted  $B$ -band light curves relating to the models Asyshell1, Asyshell2, and Asyshell3, respectively. The dashed lines are the scattered intensity. All the light curves have been scaled to the maximum light. In the lower panel, the red, blue, and orange lines are the polarization curves predicted by the models Asyshell1, Asyshell2, and Asyshell3, respectively. The parameter values of these three axisymmetric shell models are shown in Table 3.

and  $F775W$  bands. The corresponding degrees of polarization in  $F606W$  and  $F775W$  bands are about 0.65% and 0.6%, respectively. Multiband polarimetry during such a late phase could provide an important probe to investigate the dust properties of CSM around SN 2014J, since the relationships between the scattering cross section and wavelengths are different for different dust grains. For simplicity, we considered two CS models with different dust radii. The first one is just the model Asyshell3 as shown in Table 3 with the same dust radius of  $0.05 \mu\text{m}$ . The other one has the same geometric distribution and same observing angle ( $\theta_{\text{obs}} = 40^\circ$ ) as model Asyshell3 but a different dust radius ( $0.1 \mu\text{m}$ ) and different  $B$ -band optical depth ( $\tau = 0.24$ ). This slightly different optical depth can induce the model with a dust radius of  $0.1 \mu\text{m}$  to match the  $B$ -band light curve of SN 2014J as the model Asyshell3 does shown in Figure 9. We adopted the observed spectra and light curves of SN 2011fe (Zhang et al. 2016) to generate the spectral template covering the late phase to +300 days after maximum light. To reduce the calculation time, the spectropolarimetry predicted by our models spans 46 wavelengths from 350 nm to 800 nm. As shown in Figure 10, we prefer the CS dust with a radius of  $0.05 \mu\text{m}$  for matching the multiband polarization signals.

Indeed, precise polarization requires the use of large-aperture telescopes. At late times when we expect significant

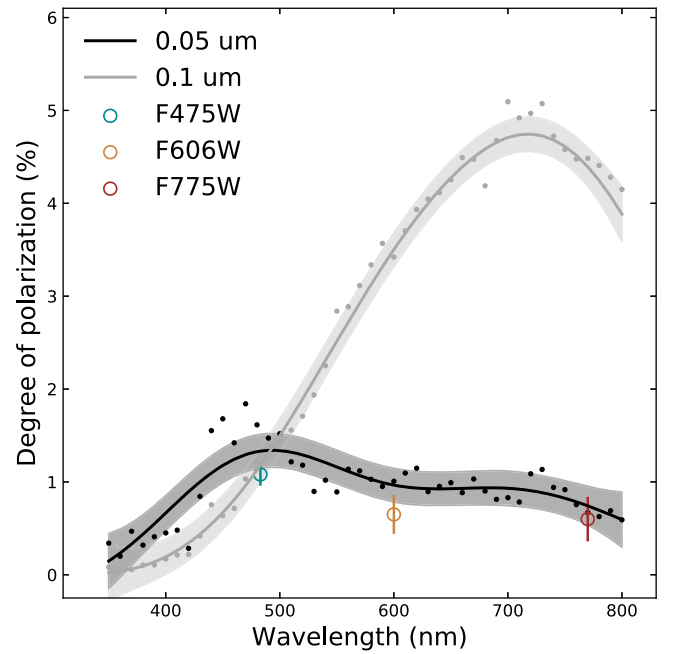


**Figure 10.** The cyan, yellow, and brown symbols are the observed polarizations of SN 2014J during 277 days after the peak brightness for HST  $F475W$ ,  $F606W$ , and  $F775W$  bands from Yang et al. (2018), respectively. The black and gray circles are polarization predicted by the models with dust radii of  $0.05 \mu\text{m}$  and  $0.1 \mu\text{m}$ , respectively. The black and gray lines are the smoothed lines from Gaussian process fitting (Pedregosa et al. 2011), and the corresponding shaded regions are the  $1\sigma$  standard deviation.

polarization evolution (50–300 days past the maximum light), SNe Ia will be more than 3.5 magnitudes dimmer than at peak light. Nonetheless, a large number of nearby SNe Ia have been routinely found by recent SN surveys, making such a program feasible.

## 5. Conclusions

This paper explores systematically the influence of dusty CSM on the light curves and polarizations of SNe Ia. We first calculated the scattering kernel functions for the Stokes parameters and then constructed the light and polarization curves by convolving the spectral template of SNe Ia with the corresponding kernel functions to obtain the model light and polarization curves. The kernel functions characterize the radiative transfer process for SNe Ia located in a dusty environment and are obtained with the Monte Carlo method. We adopted the Mie scattering theory to calculate the dust scattering cross section, albedo, and scattering matrix based on the refractive index and the specific size distribution of silicate dust. We simulated a large number of geometric model grids to study the similarities among the kernel functions of intensity between +20 and +100 days (Figure 2). Our study shows the kernel functions of the Stokes parameter for linear polarization ( $Q$ ) to be very sensitive to the geometric distribution of the dust (Figure 3). As a result, dust distributions that predict similar light curves can be more efficiently distinguished if detailed time evolution of polarization can be acquired (Figure 5). Our study shows that a time sequence of broadband polarimetry is a more powerful probe for determining the dust geometry than detailed spectropolarimetry but with less time coverage. We also compared the results between our studies and those of Bulla et al. (2018), and found that shell models with

considerably different distance scales can fit the time dependence of the  $E(B - V)$  curves (Figure 8); we argue that the location of the dust grains responsible for any time-varying reddening of SNe Ia cannot be determined reliably based on photometric optical data alone. Late-time polarimetry, especially broadband polarimetry from a few months to over a year, can be of great value in setting limits on the elusive CS dust around SNe Ia.

This work is supported by the National Natural Science Foundation of China (11761141001) and Key Research Program of Frontier Sciences of Chinese Academy of Sciences (QYZDY-SSW-SLH010). X. W. is supported by National Natural Science Foundation of China (NSFC grants 12033003 and 11633002). This work is partially supported by the Scholar Program of Beijing Academy of Science and Technology (DZ: BS202002). We thank M. Bulla, Lingzhi Wang, and Y. Yang for sharing the data used in this paper. L. W. acknowledges support from the NSF grant AST-1817099.

### ORCID iDs

Maokai Hu  <https://orcid.org/0000-0003-3031-6105>  
 Lifan Wang  <https://orcid.org/0000-0001-7092-9374>  
 Xiaofeng Wang  <https://orcid.org/0000-0002-7334-2357>

### References

Aldering, G., Antilogus, P., Bailey, S., et al. 2006, *ApJ*, 650, 510  
 Amanullah, R., Johansson, J., Goobar, A., et al. 2015, *MNRAS*, 453, 3300  
 Bianchi, S., Ferrara, A., & Giovanardi, C. 1996, *ApJ*, 465, 127  
 Blondin, S., Prieto, J. L., Patat, F., et al. 2009, *ApJ*, 693, 207  
 Bulla, M., Goobar, A., & Dhawan, S. 2018, *MNRAS*, 479, 3663  
 Chandrasekhar, S. 1950, *Radiative Transfer* (Mineola, NY: Dover Publications)  
 Chevalier, R. A. 1986, *ApJ*, 308, 225  
 Chomiuk, L., Soderberg, A. M., Chevalier, R. A., et al. 2016, *ApJ*, 821, 119  
 Chu, M. R., Cikota, A., Baade, D., et al. 2022, *MNRAS*, 509, 6028  
 Cikota, A., Patat, F., Wang, L., et al. 2019, *MNRAS*, 490, 578  
 Crotts, A. P. S. 2015, *ApJL*, 804, L37  
 Crotts, A. P. S., & Yourdon, D. 2008, *ApJ*, 689, 1186  
 De Geyter, G., Baes, M., Fritz, J., & Camps, P. 2013, *A&A*, 550, A74  
 Ding, J., Wang, L., Brown, P., & Yang, P. 2021, *ApJ*, 919, 104  
 Draine, B. T. 2003, *ApJ*, 598, 1017  
 Draine, B. T., & Lee, H. M. 1984, *ApJ*, 285, 89  
 Foley, R. J., Fox, O. D., McCully, C., et al. 2014, *MNRAS*, 443, 2887  
 Förster, F., González-Gaitán, S., Anderson, J., et al. 2012, *ApJL*, 754, L21  
 Fox, O. D., Silverman, J. M., Filippenko, A. V., et al. 2015, *MNRAS*, 447, 772  
 Gao, J., Jiang, B. W., Li, A., Li, J., & Wang, X. 2015, *ApJL*, 807, L26  
 Gao, W., Zhao, R., Gao, J., Jiang, B., & Li, J. 2020, *P&SS*, 183, 104627  
 Goobar, A. 2008, *ApJL*, 686, L103  
 Gordon, K. D., Misselt, K. A., Witt, A. N., & Clayton, G. C. 2001, *ApJ*, 551, 269  
 Hamuy, M., Phillips, M. M., Suntzeff, N. B., et al. 2003, *Natur*, 424, 651  
 He, S., Wang, L., & Huang, J. Z. 2018, *ApJ*, 857, 110  
 Henyey, L. G., & Greenstein, J. L. 1941, *ApJ*, 93, 70

Hillebrandt, W., & Niemeyer, J. C. 2000, *ARA&A*, 38, 191  
 Howell, D. A. 2011, *NatCo*, 2, 350  
 Hsiao, E. Y., Conley, A., Howell, D. A., et al. 2007, *ApJ*, 663, 1187  
 Iben, I. J., & Tutukov, A. V. 1984, *ApJS*, 54, 335  
 Inserra, C., Fraser, M., Smartt, S. J., et al. 2016, *MNRAS*, 459, 2721  
 Johansson, J., Goobar, A., Kasliwal, M. M., et al. 2017, *MNRAS*, 466, 3442  
 Kawabata, K. S., Akitaya, H., Yamanaka, M., et al. 2014, *ApJL*, 795, L4  
 Li, W., Wang, X., Hu, M., et al. 2019, *ApJ*, 882, 30  
 Lundqvist, P., Kundu, E., Pérez-Torres, M. A., et al. 2020, *ApJ*, 890, 159  
 Lundqvist, P., Nyholm, A., Taddia, F., et al. 2015, *A&A*, 577, A39  
 Maguire, K., Sullivan, M., Patat, F., et al. 2013, *MNRAS*, 436, 222  
 Maoz, D., Mannucci, F., & Nelemans, G. 2014, *ARA&A*, 52, 107  
 Margutti, R., Parent, J., Kamble, A., et al. 2014, *ApJ*, 790, 52  
 Marion, G. H., Sand, D. J., Hsiao, E. Y., et al. 2015, *ApJ*, 798, 39  
 Mauerhan, J. C., Van Dyk, S. D., Johansson, J., et al. 2017, *ApJ*, 834, 118  
 Moore, K., & Bildsten, L. 2012, *ApJ*, 761, 182  
 Nagao, T., Maeda, K., & Tanaka, M. 2017, *ApJ*, 847, 111  
 Nagao, T., Maeda, K., & Yamanaka, M. 2018, *MNRAS*, 476, 4806  
 Nomoto, K. 1982, *ApJ*, 253, 798  
 Nozawa, T., Wakita, S., Hasegawa, Y., & Kozasa, T. 2015, *ApJL*, 811, L39  
 Ofek, E. O., Cameron, P. B., Kasliwal, M. M., et al. 2007, *ApJL*, 659, L13  
 Patat, F. 2005, *MNRAS*, 357, 1161  
 Patat, F., Chandra, P., Chevalier, R., et al. 2007, *Sci*, 317, 924  
 Patat, F., Höflich, P., Baade, D., et al. 2012, *A&A*, 545, A7  
 Pedregosa, F., Varouaux, G., Gramfort, A., et al. 2011, *JMLR*, 12, 2825  
 Peest, C., Camps, P., Stalevski, M., Baes, M., & Siebenmorgen, R. 2017, *A&A*, 601, A92  
 Pérez-Torres, M. A., Lundqvist, P., Beswick, R. J., et al. 2014, *ApJ*, 792, 38  
 Perlmutter, S., Aldering, G., Goldhaber, G., et al. 1999, *ApJ*, 517, 565  
 Porter, A. L., Leising, M. D., Williams, G. G., et al. 2016, *ApJ*, 828, 24  
 Rest, A., Matheson, T., Blondin, S., et al. 2008, *ApJ*, 680, 1137  
 Rest, A., Prieto, J. L., Walborn, N. R., et al. 2012, *Natur*, 482, 375  
 Riess, A. G., Filippenko, A. V., Challis, P., et al. 1998, *AJ*, 116, 1009  
 Riess, A. G., Strolger, L.-G., Casertano, S., et al. 2007, *ApJ*, 659, 98  
 Sand, D. J., Hsiao, E. Y., Banerjee, D. P. K., et al. 2016, *ApJL*, 822, L16  
 Shen, K. J., Guillochon, J., & Foley, R. J. 2013, *ApJL*, 770, L35  
 Simon, J. D., Gal-Yam, A., Gnat, O., et al. 2009, *ApJ*, 702, 1157  
 Srivastav, S., Ninan, J. P., Kumar, B., et al. 2016, *MNRAS*, 457, 1000  
 Steinacker, J., Baes, M., & Gordon, K. D. 2013, *ARA&A*, 51, 63  
 Sternberg, A., Gal-Yam, A., Simon, J. D., et al. 2011, *Sci*, 333, 856  
 Taddia, F., Stritzinger, M. D., Phillips, M. M., et al. 2012, *A&A*, 545, L7  
 Tanaka, M., Kawabata, K. S., Yamanaka, M., et al. 2010, *ApJ*, 714, 1209  
 Wang, L. 2005, *ApJL*, 635, L33  
 Wang, L., Baade, D., Höflich, P., et al. 2004, *ApJL*, 604, L53  
 Wang, L., Goldhaber, G., Aldering, G., & Perlmutter, S. 2003, *ApJ*, 590, 944  
 Wang, L., & Wheeler, J. C. 1996, *ApJL*, 462, L27  
 Wang, L., & Wheeler, J. C. 2008, *ARA&A*, 46, 433  
 Wang, X., Chen, J., Wang, L., et al. 2019, *ApJ*, 882, 120  
 Wang, X., Filippenko, A. V., Ganeshalingam, M., et al. 2009, *ApJL*, 699, L139  
 Wang, X., Li, W., Filippenko, A. V., et al. 2008a, *ApJ*, 677, 1060  
 Wang, X., Li, W., Filippenko, A. V., et al. 2008b, *ApJ*, 675, 626  
 Wang, X., Wang, L., Pain, R., Zhou, X., & Li, Z. 2006, *ApJ*, 645, 488  
 Webbink, R. F. 1984, *ApJ*, 277, 355  
 Whelan, J., & Iben, I. J. 1973, *ApJ*, 186, 1007  
 Witt, A. N. 1977, *ApJS*, 35, 1  
 Wolf, S., & Voshchinnikov, N. V. 2004, *CoPhC*, 162, 113  
 Wood-Vasey, W. M., Wang, L., & Aldering, G. 2004, *ApJ*, 616, 339  
 Yang, Y., Wang, L., Baade, D., et al. 2017, *ApJ*, 834, 60  
 Yang, Y., Wang, L., Baade, D., et al. 2018, *ApJ*, 854, 55  
 Zhang, K., Wang, X., Zhang, J., et al. 2016, *ApJ*, 820, 67